AGU PUBLICATIONS

Geochemistry, Geophysics, Geosystems

RESEARCH ARTICLE
10.1002/2016GC006300

Special Section:
Magnetism From Atomic to Planetary Scales: Physical Principles and Interdisciplinary Applications in Geo- and Planetary Sciences

Magnetic record of deglaciation using FORC-PCA, sortable-silt grain size, and magnetic excursion at 26 ka, from the Rockall Trough (NE Atlantic)

J. E. T. Channell[1], R. J. Harrison[2], I. Lascu[2], I. N. McCave[2], F. D. Hibbert[3], and W. E. N. Austin[4,5]

[1]Department of Geological Sciences, University of Florida, Gainesville, Florida, USA, [2]Department of Earth Sciences, University of Cambridge, Cambridge, UK, [3]Research School of Earth Sciences, Australian National University, Canberra, Australian Capital Territory, Australia, [4]School of Geography and Geosciences, University of St. Andrews, St. Andrews, UK, [5]Scottish Marine Institute, Scottish Association for Marine Science, Oban, UK

Abstract Core MD04-2822 from the Rockall Trough has apparent sedimentation rates of ~ 1 m/kyr during the last deglaciation (Termination I). Component magnetization directions indicate a magnetic excursion at 16.3 m depth in the core, corresponding to an age of 26.5 ka, implying an excursion duration of ~350 years. Across Termination I, the mean grain size of sortable silt implies reduced bottom-current velocity in the Younger Dryas and Heinrich Stadial (HS)−1A, and increased velocities during the Bølling-Allerød warm period. Standard bulk magnetic parameters imply fining of magnetic grain size from the mid-Younger Dryas (~12 ka) until ~ 8 ka. First-order reversal curves (FORCs) were analyzed using ridge extraction to differentiate single domain (SD) from background (detrital) components. Principal component analysis (FORC-PCA) was then used to discriminate three end members corresponding to SD, pseudo-single domain (PSD), and multidomain (MD) magnetite. The fining of bulk magnetic grain size from 12 to 8 ka is due to reduction in concentration of detrital (PSD + MD) magnetite, superimposed on a relatively uniform concentration of SD magnetite produced by magnetotactic bacteria. The decrease in PSD+MD magnetite concentration from 12 to 8 ka is synchronized with increase in benthic $\delta^{13}C$, and with major (~70 m) regional sea-level rise, and may therefore be related to detrital sources on the shelf that had reduced influence as sea level rose, and to bottom-water reorganization as Northern Source Water (NSW) replaced Southern Source Water (SSW).

Key Points:
- FORC-PCA as a new magnetic grain-size discriminator
- Relationship of magnetic and sortable-silt grain size proxies over Termination I
- New putative magnetic excursion at 26.5 ka

Supporting Information:
- Supporting Information S1

Correspondence to:
J. E. T. Channell,
jetc@ufl.edu

Citation:
Channell, J. E. T., R. J. Harrison, I. Lascu, I. N. McCave, F. D. Hibbert, and W. E. N. Austin (2016), Magnetic record of deglaciation using FORC-PCA, sortable-silt grain size, and magnetic excursion at 26 ka, from the Rockall Trough (NE Atlantic), *Geochem. Geophys. Geosyst.*, *17*, doi:10.1002/2016GC006300.

Received 5 FEB 2016
Accepted 28 APR 2016
Accepted article online 2 MAY 2016

1. Introduction

Core MD04-2822 from the Rockall Trough (Figure 1), collected from the RV *Marion Dufresne* in 2004, is ~37 m long and extends back to ~195 ka [*Hibbert et al.*, 2010]. Sedimentation rates are highly variable, declining to <5 cm/kyr in marine isotope stage (MIS) 5, but exceeding 1 m/kyr in MIS 2 and the transition into the Holocene (Termination I), although apparent sedimentation rates may be influenced by "stretching" that affects the upper part of the majority of MD (*Marion Dufresne*) cores [*Skinner and McCave*, 2003; *Széréméta et al.*, 2004]. Core MD04-2822 is from the distal margin of the Barra-Donegal fan (56° 50.54 N, 11° 22.96 W, 2344 m water depth). The Barra-Donegal Fan is the most southerly glacial fan on the NW European continental margin comprising debris flow lobes and glaciomarine sediments fed by Pleistocene ice streams [*Stoker*, 1995; *Armishaw et al.*, 2000; *Knutz et al.*, 2001]. Deep ocean circulation in this region changed during Termination I as Southern Source Water (SSW) reached water depths as shallow as ~2000 m during the Last Glacial Maximum (LGM) [*Curry and Oppo*, 2005], and was replaced during Termination I by North East Atlantic Deep Water (NEADW) with a component of Wyville-Thomson Ridge Overflow Water (WTOW) and Labrador Sea Water (LSW) (Figure 1). Southern Source Water (SSW) is found today in the deepest portion of the Trough (below 3000 m) with a pronounced vertical silicate gradient denoting the mixing of underlying SSW with NEADW, and superimposed southwesterly flow of WTOW along the western side Rockall Trough [*New and Smythe-Wright*, 2001]. Core MD04-2822 comprises clays and silts with minor sand [*Hibbert et al.*, 2010]. The attraction of this core for magnetic studies lies in its precise chronology, based on radiocarbon, tephra, benthic $\delta^{18}O$, and correlation of sea-surface temperature (SST) proxies to ice-core records, as well as the relatively high sedimentation rates in MIS 2 and during Termination I.

Variations in magnetic concentration parameters in North Atlantic sediments deposited over the last glacial cycle have been have been attributed to changes in transport of magnetic particles by deep-sea currents

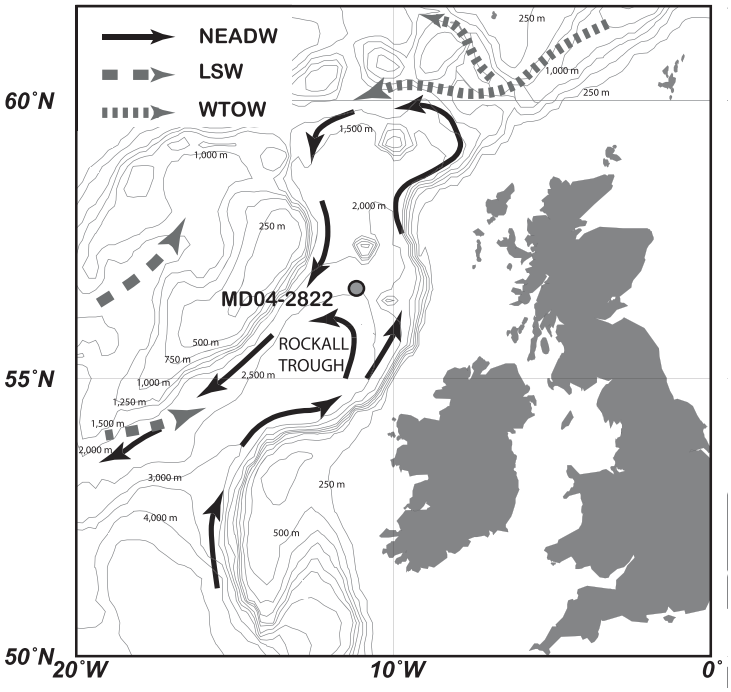

Figure 1. Location of Core MD04-2822 in the Rockall Trough. Modern deep-water flow comprises NE Atlantic Deep Water (NEADW), Labrador Sea Water (LSW), and Wyville-Thomson Ridge (at 60°N) Overflow Water (WTOW) (figure modified after *Knutz et al*. [2002]).

[e.g., *Kissel et al*., 1999]. A north to south reduction in both magnetic concentration and magnetic grain size in Holocene sediments along the axis of the Gardar/Bjorn drifts, over a distance of ~2000 km, has been attributed to down-stream transport of magnetic particles by deep-sea currents flowing from detrital sources along the Iceland-Scotland ridge [*Kissel et al*., 2009]. Also in Holocene sediments from the Gardar Drift, magnetic susceptibility tracks the mean grain size of sortable silt, implying that magnetic susceptibility in this region is a monitor of bottom-current strength [*Kissel et al*., 2013]. Similarly, *Snowball and Moros* [2003] found that magnetic concentration and grain size over the last glacial cycle from the central Gardar Drift, track the means of the 0.5–10 μm and 0.5–20 μm particle-size fractions, again implying a link between magnetic concentration, magnetic grain size, and bottom-current velocity.

Here we report the natural remanent magnetization (NRM), including the presence of a magnetic excursion at ~26 ka, and magnetic and physical granulometry, of Core MD04-2822. Measurements are from u-channel samples, continuous 2 × 2 × 150 cm^3 samples encased in plastic with a clip-on lid constituting one of the sides, collected from each (150 cm) core section. In addition, 7 cm^3 discrete samples were collected across the supposed magnetic excursion, and toothpick samples for magnetic hysteresis measurements and First-Order Reversal Curves (FORCs) were collected throughout the section but particularly over Termination I.

This study represents the first application of FORC-PCA, a new method of magnetic unmixing that uses principle component analysis (PCA) applied to FORC diagrams. We compare this method with more traditional magnetic grain size proxies, and demonstrate that FORC-PCA leads to an improved understanding of how magnetic variations are linked to underlying geological processes. The results also contribute to the controversial issue of the age and existence of magnetic excursions younger than the Laschamp excursion at ~41 ka, and provide a new perspective on the relationship between magnetic and physical grain size in North Atlantic sediments over the last glacial cycle.

2. Age Model

The chronology of Core MD04-2822 was originally based on AMS radiocarbon dates, benthic $\delta^{18}O$ from *Cibicidoides wuellerstorfi*, and percent *Neogloboquadrina pachyderma* (sin.) as a sea-surface temperature

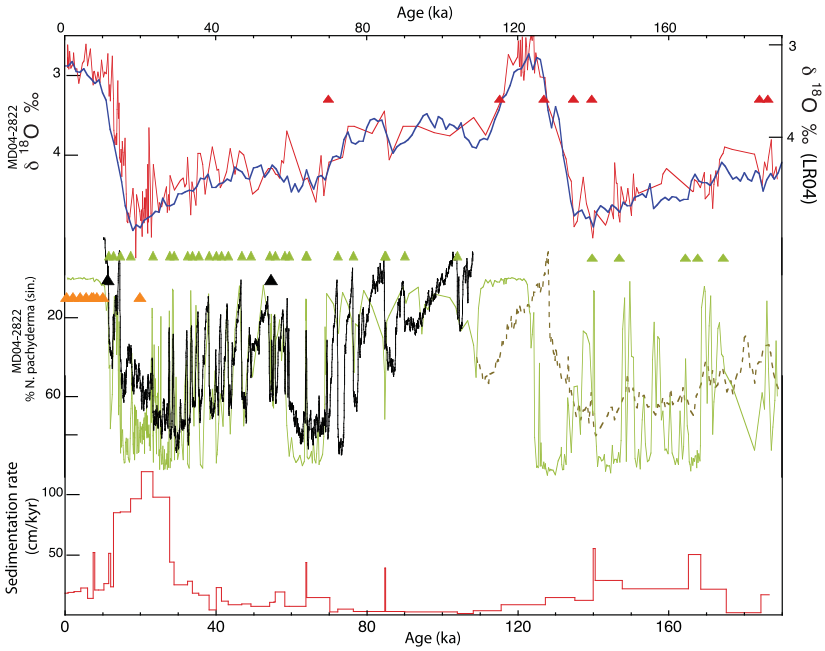

Figure 2. Core MD04-2822: (a) Benthic oxygen isotope record (red) compared to the LR04 $\delta^{18}O$ stack (blue) [*Lisiecki and Raymo*, 2005], (b) Percent *N. pachyderma* (sin.) (green) compared to the NGRIP Greenland oxygen isotope record with 10 point smoothing (black) for the last 115 kyr on the GICC05 timescale [*Rasmussen et al*., 2014 and references therein), and beyond 120 ka, to the Antarctic (EDC) methane record (dashed brown) on the AICC2012 chronology [*Bazin et al*., 2013]. (c) Inferred sedimentation rates. Colored triangles indicate sources of age control: radiocarbon (orange), tephra (black), correlation of benthic oxygen isotope data to the LR04 $\delta^{18}O$ stack (red), and correlation of percent *N. pachyderma* (sin.) to NGRIP $\delta^{18}O$ and to Antarctic (EDC) methane (green).

(SST) proxy linked to the Greenland $\delta^{18}O$ and Antarctic methane records [*Hibbert et al*., 2010]. The age model has now been strengthened by: (1) recognition of both the Vedde Ash (I-RHY-I component) at 12.17 ka and North Atlantic Ash Zone (NAAZ) II at 55.38 ka. (2) Use of percent *N. pachyderma* (sin.) to link the core to Greenland ice core (NGRIP) $\delta^{18}O$, using updated ages for the NGRIP ice core on the GICC05 timescale [*Rasmussen et al*., 2014 and references therein), and beyond 140 ka, the use of the Antarctic AICC2012 chronology for the EDC ice core [*Bazin et al*., 2013] to perform this linkage through methane tuning. (3) Additional AMS ^{14}C dating [*Austin and Hibbert*, 2012; *Hibbert et al*., 2014] (supporting information Table S1) calibrated using the Marine13 calibration curve [*Reimer et al*., 2013] using OxCal (version 4.2; Bronk Ramsey, 2009). We use $\Delta R = 0 \pm 50$ years to calibrate the Holocene samples; at present, the average (n=6) regional $\Delta R = -1 \pm 52$ years [*Harkness*, 1983; *Hãykansson*, 1984; *Olsson*, 1980]. Locally, the marine reservoir increased to 700 years [*Austin et al*., 1995] during the Younger Dryas, with glacial values of >1000 years proposed [cf. *Waelbroeck et al*., 2001]. We used $\Delta R = 700 \pm 500$ years for the single *N. pachyderma* (sin.) date (SUERC 12920) to account for changes in glacial surface oceanography. The similarity of the radiocarbon determinations from the upper 15.5 cm of the core (supporting information Table S1) results from the biological mixing of sediments. Consequently, we set the bottom of the surface mixed layer (i.e., the limit of the biologically mixed layer) to a depth of 15.5 cm for MD04-2822 with an age derived from the average of three calibrated ^{14}C dates [cf. *Brown et al*., 2001]. Age uncertainty estimates (supporting information Figure S1, Tables S1, and S2) were determined for each tie-point using a mean-squared estimate that included age uncertainties associated with ice-core chronologies, and the error in the position of the tie-point within the marine record due to sample spacing, core resolution, and sediment bioturbation. We combined the tie-point age and depth information using a Bayesian deposition model (the OxCal "Poisson" function, allowing sedimentation rates to vary widely) [*Bronk Ramsey and Lee*, 2013] to derive age control between tie-points. The overall agreement between the model priors and posteriors is high: agreement index > 78% for all dates in the MD04-2822 Poisson model (acceptance threshold > 60%) [*Bronk Ramsey*, 2008]. Sedimentation rates are highly variable with sedimentation rate maxima in MIS 2 and across Termination I (Figure 2).

3. Magnetic Methods

Continuous u-channel samples were collected from the 1.5 m-long archive-half sections of Core MD04-2822. Measurements of natural remanent magnetization (NRM) of u-channel samples were made at 1 cm intervals, with a 10 cm leader and trailer at the top and base of each u-channel sample, using a 2G Enterprises pass-through magnetometer at the University of Florida that has Gaussian-shaped response functions with width at half-height of ~4.5 cm [*Weeks et al*., 1993; *Guyodo et al*., 2002]. After initial NRM measurement of u-channel samples, stepwise alternating field (AF) demagnetization was carried out in 5 mT increments in the 10–60 mT peak field interval, and in 10 mT increments in the 60–100 mT interval, using tracking speeds of 10 cm/s. Component magnetizations were computed each 1 cm for a uniform 20–80 mT demagnetization interval using the standard least squares method [*Kirschvink*, 1980] without anchoring to the origin of the orthogonal projections, using UPmag software [*Xuan and Channell*, 2009].

The apparent excursion recorded in the u-channel record of Core MD04-2822 was also sampled using cubic (7 cm^3) plastic boxes, collected from alongside the u-channel trough, in order to further investigate the excursion interval. Discrete samples were subject to either stepwise alternating field (AF) or thermal demagnetization after initial measurement of NRM. For AF demagnetization, increments were 5 mT in the 5–95 mT peak AF range. Thermal demagnetization experiments were conducted by measuring NRM before thermal demagnetization, then again after wrapping samples in Al foil, and then after demagnetization of wrapped samples in 25°C steps in the 75–600°C temperature range. Magnetization directions were measured on a 2G Enterprises discrete-sample magnetometer, and component magnetization directions were determined using at least 10 concurrent demagnetization steps without anchoring to the origin of the orthogonal projections. After AF demagnetization of the NRM of 7 cm^3 discrete samples recording the apparent magnetic excursion (Figure 5), these 40 samples were dried in field-free space, extracted from their plastic cubes, and wrapped in Al-foil. The remanent magnetization was measured before and after wrapping, and then three-axis IRMs were imposed sequentially and orthogonally for each sample using DC fields of 1.2 T, 0.3 T, and 0.1 T [see *Lowrie*, 1990].

After NRM measurement of u-channel samples, anhysteretic remanent magnetization (ARM) was imposed on each u-channel in a DC field of 50 μT and an AF field decaying from a peak value of 100 mT, and then this ARM was demagnetized at the same steps used to demagnetize NRM. The slope of NRM versus ARM during stepwise demagnetization was used as a proxy for relative paleontensity (RPI), the intensity of the geomagnetic field at time of sediment deposition. This RPI proxy was augmented by two additional proxies (slopes), also measured at 1 cm intervals down-core: NRM demagnetization versus ARM acquisition (ARMAQ), and NRM demagnetization versus demagnetization of isothermal remanent magnetization (IRM) acquired in a DC field of 1T [e.g., *Channell et al*., 2014]. Ideally, ARM and IRM activate the same population of magnetite grains that carry NRM, and hence normalizes NRM intensity for changes in the concentration of NRM-carrying grains downcore. Volume susceptibility (κ) was measured at 1 cm intervals using a susceptibility track designed for u-channel samples that has a Gaussian-shaped response function, with width at half height of ~4 cm, similar to the response function of the u-channel magnetometer [*Thomas et al*., 2003]. Following *Banerjee et al*. [1981] and *King et al*. [1983], the ratio of anhysteretic susceptibility (κ_{ARM}, ARM intensity normalized by the DC bias field used to acquire the ARM) to susceptibility (κ) can be used to estimate grain size in magnetite. The measurement of IRM, acquired in DC fields of 0.3 T and 1 T ($IRM_{0.3T}$ and IRM_{1T}), allows us to calculate a "forward S-ratio" [see *Heslop*, 2009] calculated as the ratio: $IRM_{0.3T}/IRM_{1T}$. The S-ratio is sensitive to the abundance of high-coercivity minerals such as hematite and is not primarily influenced by magnetic grain-size.

Additional mineralogical information was acquired from magnetic hysteresis data measured on a Princeton Measurements Corp. vibrating sample magnetometer (VSM) at the University of Florida. Hysteresis ratios: M_r/M_s and B_{cr}/B_c where M_r is saturation remanence, M_s is saturation magnetization, B_{cr} is coercivity of remanence, and B_c is coercive force, can be used to delineate single domain (SD), pseudo-single domain (PSD), and multidomain (MD) magnetite and to assign "mean" magnetite grain sizes through empirical and theoretical calibrations of the so-called Day plot [*Day et al*., 1977; *Carter-Stiglitz et al*., 2001; *Dunlop*, 2002; *Dunlop and Carter-Stiglitz*, 2006]. First-order reversal curves (FORCs) provide enhanced magnetic mineral and domain state discrimination [*Pike et al*., 1999; *Roberts et al*., 2000; *Muxworthy and Roberts*, 2007] and are measured by progressively saturating a small (few hundred mg) sample in a field (B_{sat}), decreasing the field to a value B_a, reversing the field, and sweeping it back to B_{sat} in a series of regular field steps (B_b). The

process is repeated for many values of B_a. The magnetization is then represented as a contour plot with axes B_c and B_u where $B_c = (B_b - B_a)/2$ and $B_u = (B_b + B_a)/2$. The contoured distribution of a FORC can be interpreted in terms of the coercivity distribution along the B_c axis. Spreading of the distribution along the B_u axis corresponds to magnetostatic interactions for SD grains or internal demagnetizing fields for MD grains, although the latter dominates in weakly magnetized deep-sea sediments, and spreading in B_u combined with low B_c can be interpreted in terms of high MD magnetite content. In general, closed peaked structures along the B_c axis are characteristic of SD grains, with contours becoming progressively more parallel to the B_u axis with grain-size coarsening. FORC diagrams were mass normalized and processed with FORCinel [*Harrison and Feinberg*, 2008] using drift correction and VARIFORC smoothing protocols described by *Egli* [2013]. Two hundred and thirteen (213) FORCs collected at 2–5 cm intervals over the 4.5–18.5 ka interval were measured using averaging time of 1 s, and a field increment of 2 mT up to a maximum applied field of 1 T. FORCs were analyzed by two methods: (1) by extraction of the ridge (SD) signal and interpolation of the background, followed by subtraction of the background from the total FORC signal, following *Egli et al*. [2010], and (2) by Principal Component Analysis (PCA) following *Lascu et al*. [2015]. FORCs were mass normalized and smoothed using $S_{c0} = 7$, $S_{c1} = 9$, $S_{b0} = 3.5$, $S_{b1} = 9$, $\lambda_c = 0.1$, and $\lambda_b = 0.1$.

4. Magnetic Excursion at ~26 ka

The maximum angular deviation (MAD) values associated with NRM component magnetization directions are generally below 10° for Core MD04-2822 (Figure 3), indicating well-defined magnetization components. Cores were not oriented in azimuth although declination is relative as the same (archive) half of the core was consistently sampled. The high mean inclination (~68°), close to that expected for a geocentric axial dipole field at the sampling site (72°), results in high variation in declination, superimposed on apparent twisting of the sediment core. An apparent magnetic excursion is observed in declination and inclination at ~16 meters below seafloor (mbsf) (Figure 3).

Magnetic excursions are brief (millennial-scale) directional aberrations of the geomagnetic field that, when optimally recorded, are often manifested as paired reversals where the virtual geomagnetic poles (VGPs) reaches high latitudes in the opposite hemisphere [*Laj and Channell*, 2007; *Channell et al*., 2012]. Magnetic excursions coincide with relative paleointensity (RPI) minima, as do long-lived reversals, and ~8 excursions have been adequately documented within the Brunhes Chron [e.g., *Laj and Channell*, 2007]. The catalog of Quaternary magnetic excursions is controversial for several reasons. Magnetic excursions are brief millennial or centennial-scale events and therefore their recording is fortuitous in sediments or volcanic rocks, and depends on the stochastic nature of sediment accumulation or volcanic eruption. Magnetic excursions are only likely to be recorded in sediments with mean sedimentation rates well in excess of 10 cm/kyr. The recording of such brief events in sediments is "filtered" by the NRM acquisition process, which results in smoothing of the signal through bioturbation in the uppermost ~10 cm, and progressive remanence acquisition below the bioturbated layer [see *Channell and Guyodo*, 2004; *Roberts and Winklhofer*, 2004; *Stoner et al*., 2013]. In addition, age dating of putative excursions is often not sufficiently robust to distinguish one excursion from another, and to conclusively ascertain that repeated observations are unequivocal observations of the same event. Furthermore, directional anomalies in NRM data may be accounted for by a myriad of nongeomagnetic causes, including drilling and sampling disturbance.

Typical orthogonal projections of demagnetization data recording the magnetic excursion from u-channel samples (AF demagnetization) and discrete samples (thermal and AF demagnetization) are illustrated in Figure 4. All orthogonal projections in Figure 4, other than Figure 4f that is an example from just above the excursion interval, show magnetization components with steep negative inclinations, implying the presence of the magnetic excursion. Across the excursion interval, component magnetization directions from u-channel samples, computed for a uniform 20–60 mT peak demagnetizing field, are associated with MAD values that are generally lower than MAD values associated with discrete samples (Figure 5), probably due to the averaging effect of the larger (u-channel) magnetometer response function and/or to increased sediment disturbance associated with discrete sampling. Nonetheless, MAD values are predominantly $<10°$ indicating moderately well-defined component magnetizations for both discrete and u-channel samples (Figure 5). Excursion component directions are observed over a ~35 cm interval from 1615–1650 cmbsf or 26.35–26.70 ka, an excursion duration of ~350 years according to the age model. Virtual geomagnetic poles (VGPs) reach high (negative) latitudes in the southern hemisphere (Figure 5) implying that the excursion

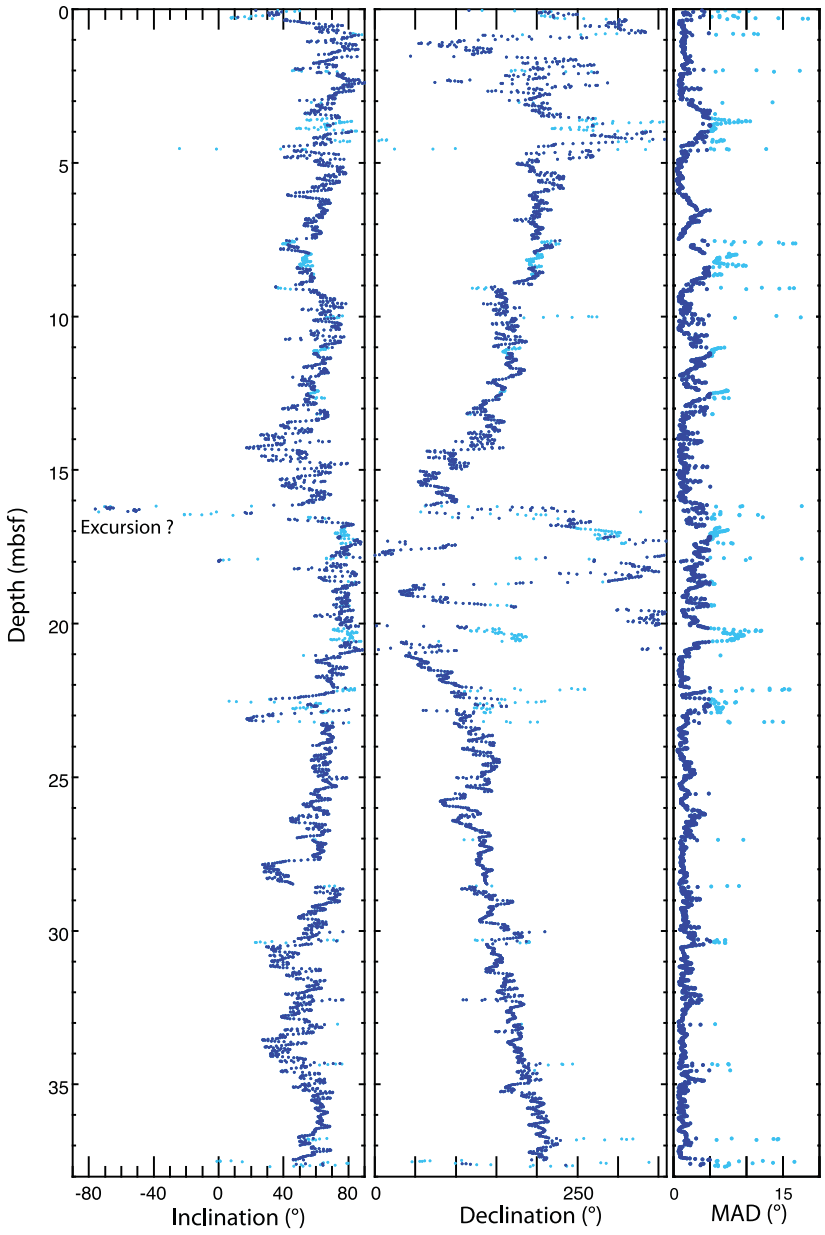

Figure 3. Component declination, inclination, and maximum angular deviation (MAD) values computed for the 20–80 mT demagnetization interval plotted versus depth (meters below seafloor, mbsf). Dark blue (light blue) symbols indicate directions associated with MAD values $<5°$ ($>5°$).

involves reversal of the Earth's main dipole field. The VGP path involves three loops, two of which precede the loop (Loop 3 in Figure 5) that takes the VGPs to highly southerly latitude.

The apparent magnetic excursion lies within a RPI minimum in Core MD04-2822 that is defined by three RPI proxies: slopes of NRM/ARM, NRM/ARMAQ, and NRM/IRM (Figure 6a). RPI minima at ~16.3, ~19.4, and ~20.6 mbsf (shaded in Figure 6a) correspond to ages of 26.5, 34.5, and 40.8 ka (shaded in Figure 6b). RPI data have lower resolution below 18 mbsf (29 ka) due to reduced sedimentation rates below 18 mbsf (29 ka) relative to the section above (Figure 2). Calibrated RPI templates, such as PISO that covers the last 1.5 Myr [*Channell et al.*, 2009], have inadequate resolution for detailed comparison with the Core MD04-2822 RPI record. On the other hand, RPI minima at ~34.5 and ~40.8 ka correspond to acceptable ages for the

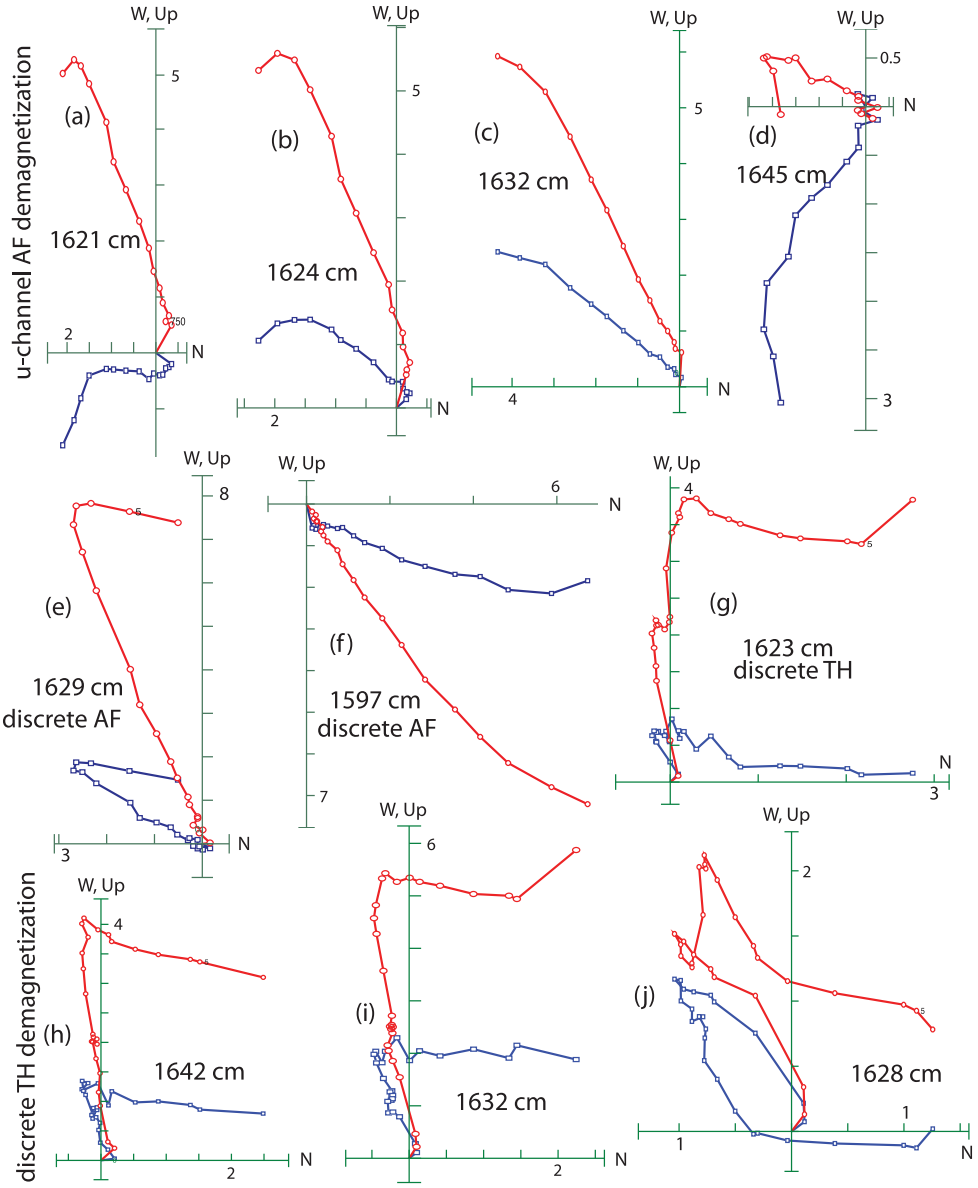

Figure 4. Orthogonal projections of demagnetization data in the vicinity of the putative magnetic excursion: (a–d) u-channel samples during alternating field demagnetization for peak fields of 10–80 mT, (e–f) 7 cm^3 discrete sample data after alternating field demagnetization for peak fields of 0–100 mT, (g–j) 7 cm^3 discrete sample data after thermal demagnetization for temperatures of 0–600°C. Red (blue) lines/symbols represent projection on the vertical (horizontal) plane. Depths below seafloor (cm) in Core MD04-2822 are given (see Figure 5 for stratigraphic sequence). Axes are scaled in mA/m.

Mono Lake and Laschamp excursions (Figure 6b), respectively, and to RPI minima derived from ice-core cosmogenic isotope flux [*Muscheler et al.*, 2005].

5. Magnetic Mineralogy

The mean of the S-ratio for Core MD04-2822 is 0.95 (std. deviations 0.05), indicating that low coercivity magnetic minerals (e.g., magnetite) are dominant. The values of (κ_{ARM}/κ) show a range of bulk magnetite grain size in the 0.1–5 μm range (Figure 7a), according to the calibration of King et al. [1983]. By comparison with measurements of unannealed sized magnetites [*Dunlop*, 2002], the Day plot indicates bulk magnetite grain

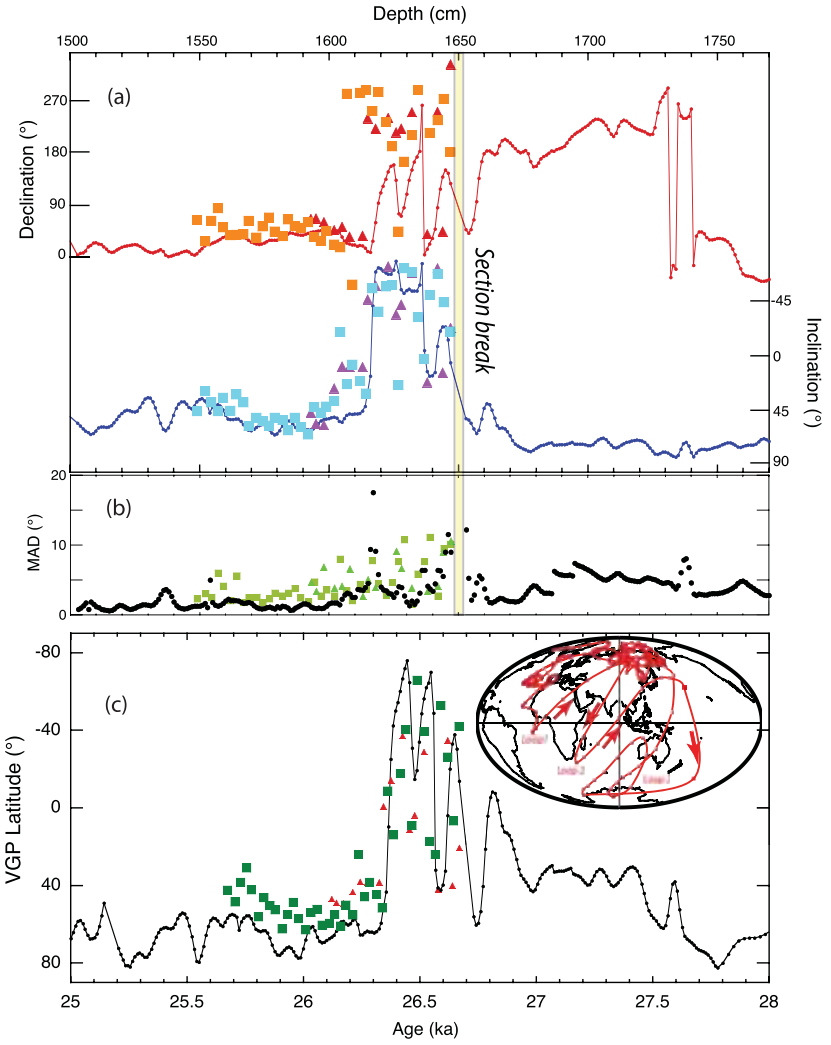

Figure 5. Core MD04-2822: (a) Component declination and inclination from u-channel samples after alternating field (AF) demagnetization (dots with line), discrete samples after AF demagnetization (squares) and thermal demagnetization (triangles) plotted versus depth. (b) Maximum angular deviation (MAD) values associated with the component directions for AF demagnetization of u-channel samples (black dots), AF demagnetization of discrete samples (green squares) and thermal demagnetization of discrete samples (green triangles). (c) Virtual geomagnetic polar (VGP) latitudes versus age for u-channel samples (black dots with line), alternating field demagnetization of discrete samples (green squares) and thermal demagnetization of discrete samples (red triangles). Location of section break indicated. Map projection inset: Virtual geomagnetic poles (VGPs) from u-channel samples during the ~26 ka magnetic excursion, indicating three VGP loops leading to VGPs at high southern latitudes during Loop 3 followed by return of VGPs to high northern latitudes.

sizes in the 0.1–5 μm range (Figure 7b), broadly consistent with the κ_{ARM} versus κ plot (Figure 7a). The displayed FORC diagram (Figure 7c) is from the excursion interval, and is typical for the glacial intervals of the core, and characterized by a mixture of SD and abundant detrital PSD + MD magnetite, consistent with the Day plot (Figure 7b). Thermal demagnetization of the three-axis IRM, imposed sequentially in DC fields of 1.2 T, 0.3 T, and 0.1 T, indicates that the magnetic mineralogy is dominated by a low-coercivity mineral that acquires its IRM in magnetizing fields of 0.1 T, and that the IRMs do not have unblocking temperatures above 600°C (Figure 7d), supporting the dominance of magnetite in the magnetic mineralogy of the excursion interval.

6. Magnetic and Physical Granulometry

In Core MD04-2822, the Holocene and MIS 5 are associated with relatively fine magnetite grain size, as indicated by the high values of the κ_{ARM}/κ grain-size parameter (Figure 8). These changes in magnetic grain-

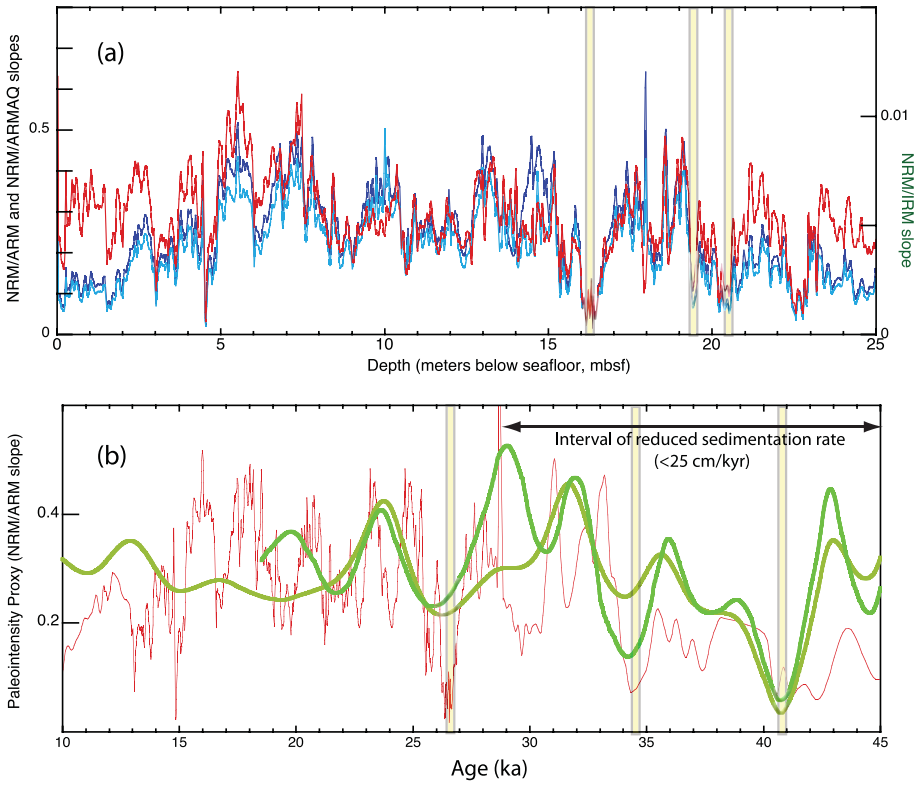

Figure 6. Core MD04-2822: (a) Slopes of NRM/ARM (dark blue), NRM/ARMAQ (light blue), and NRM/IRM (red) constituting three relative paleointensity (RPI) proxies. (b) The NRM/ARM RPI proxy (red) compared with RPI proxy determined from the flux of ^{10}Be (dark green) and ^{36}Cl (light green) in Greenland ice cores from *Muscheler et al.* [2005]. Yellow shading indicates three RPI minima in Core MD04-2822 corresponding to 26.5, 34.5, and 40.8 ka.

size correspond with shifts in $\delta^{13}C$, and with Zr/Sr and Si/Sr ratios determined by X-ray fluorescence (XRF) core scanning, that are proxies for detrital input [e.g., *Croudace et al.*, 2006]. The κ_{ARM}/κ grain-size parameter is, however, lagged by a few kyr relative to $\delta^{18}O$ over Termination I and II (Figure 8). The ARM/IRM ratio (not shown) closely mimics the κ_{ARM}/κ grain size parameter, indicating that the κ_{ARM}/κ ratio is not influenced by paramagnetic or diamagnetic contributions to susceptibility in these magnetite-bearing sediments.

These observations led us to compare the parameter commonly used to gauge bottom-current velocity, the mean sortable-silt (10–63 μm) grain size [*McCave et al.*, 1995] with magnetic grain size and concentration parameters over Termination I (Figure 9). Samples were analyzed for particle size using a Coulter Multisizer 3 equipped with a 200 μm aperture giving an optimum sizing range of 4–80 μm. Prior to analysis, carbonate and opaline silica were removed from the <63 μm grain-size fraction by treatment with dilute acetic acid (1 *M*) and heated (85°C) sodium carbonate (2 *M*). The precision of Coulter counter measurements of sortable silt mean size ($\overline{SS}$) is ±1.5% when SS concentrations exceed 5% of the <63 μm fraction [*Bianchi et al.*, 1999; *McCave and Hall*, 2006]. Whereas the κ_{ARM}/κ magnetic grain-size parameter indicates a progressive fining of magnetite grain size across the Termination (Figure 9a), the mean sortable-silt parameter indicates no progressive change across the Termination, but rather sortable-silt fining during Heinrich Stadial (HS)−1A followed by relative coarsening in the Bølling-Allerød warm period and then fining in the Younger Dryas (Figure 9b). The traditional interpretation would be that reduced/increased vigor of bottom currents led to reduced/increased mean sortable-silt grain size during cold and warm intervals, respectively. The increase in κ_{ARM}/κ from the Younger Dryas (YD) is due to increases in ARM intensity and susceptibility (κ) at the onset of HS-1A and the subsequent increase and decrease in ARM intensity and susceptibility, respectively, from the end of the Bølling-Allerød warm period (Figure 9a).

The decoupling of the sortable-silt grain size and magnetic grain-size parameters (Figure 9) is due to the fact that magnetic and sortable-silt parameters are sensitive to very different grain-size ranges. The

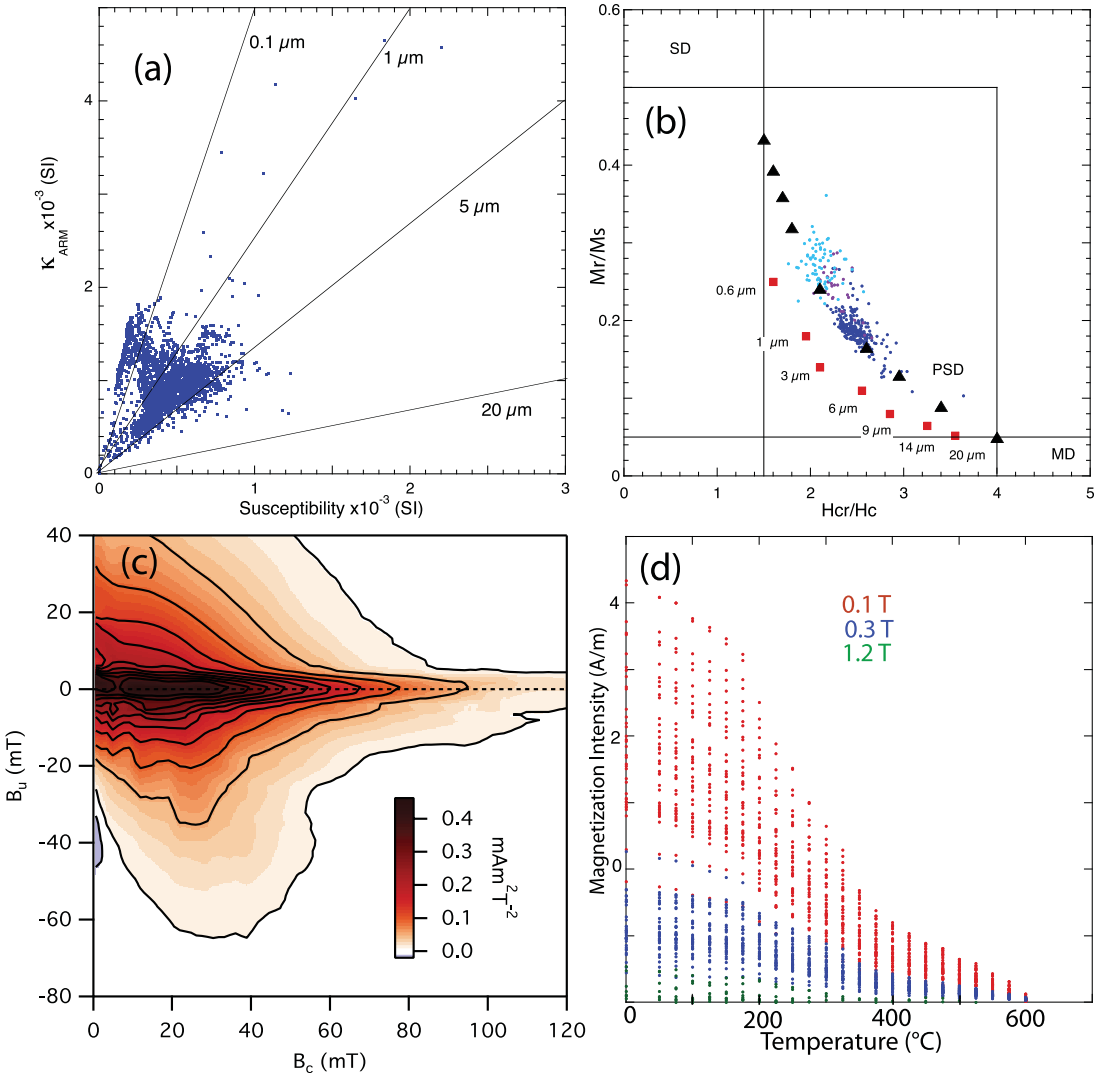

Figure 7. Core MD04-2822: (a) Plot of anhysteretic susceptibility (κ_{ARM}) against susceptibility (κ) (blue dots) with the calibration of magnetite grain size from King et al. [1983]. (b) Hysteresis ratio plot after Day et al. [1977], with ratios from top section (0–150 cm) in light blue, section 2 (150–300 cm or 8.1–13.0 ka) in purple, and below section 2 in dark blue. Black triangles: magnetite grain-size mixing line between the single domain (SD) and multidomain (MD) fields. Red squares: hysteresis ratios from crushed, sized (unannealed) natural titanomagnetite [*Dunlop*, 2002]. (c) FORC diagram for sample from 1632 cm below seafloor in the magnetic excursion interval (see Figure 5). (d) Thermal demagnetization of a three-axis IRM applied to 40 samples from the excursion interval using orthogonal magnetizing fields of 0.1 T (red), 0.3 T (blue), and 1.2 T (green).

sortable-silt parameter is sensitive to the 10–63 μm grain size (of silicates and silica) and the magnetic parameters are mainly sensitive to the submicron to few micron grains of one mineral (magnetite) that may occur as isolated grains or be incorporated as inclusions in other minerals. Our interpretation is that the sortable-silt parameter is, indeed, a monitor of bottom-current strength and is sensitive to millennial-scale fluctuation in bottom currents across the Termination. The magnetic grain-size parameters, on the other hand, are largely sensitive to grain sizes below the size associated with hydrodynamically sensitive grains that monitor bottom-current velocity.

The M_r/M_s ratios, determined from individual hysteresis loops after subtraction of the paramagnetic influence, indicate fining of magnetite grain size at Termination I (Figure 9c) during the interval of fining indicated by the κ_{ARM}/κ parameter (Figure 9a).

Extraction of the FORC central-ridge was performed by masking the central ridge, defined here as the region with $|B_u| < 5$ mT (Figure 10), and applying locally weighted regression smoothing [*Harrison and*

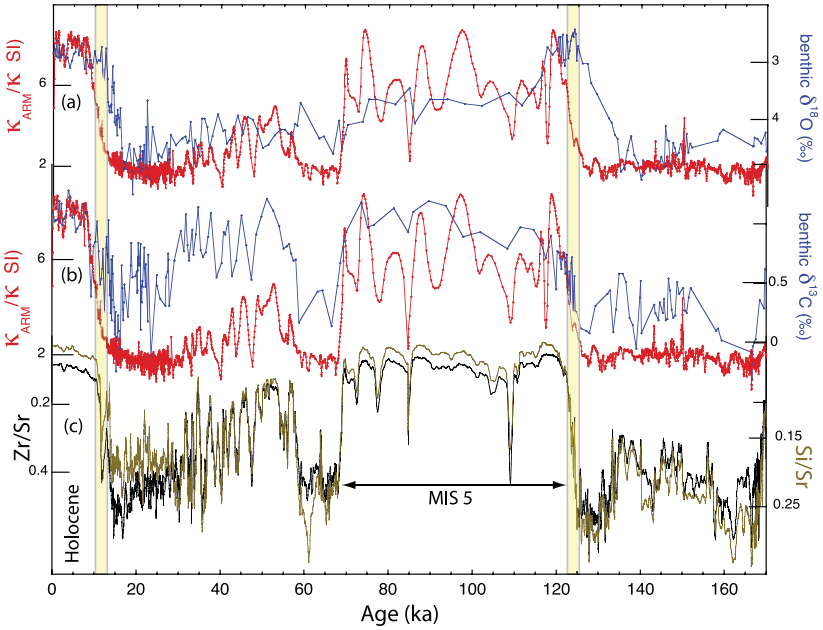

Figure 8. Core MD04-2822: (a) κ_{ARM}/κ magnetic grain size proxy (red) and benthic $\delta^{18}O$ (blue) (b) κ_{ARM}/κ (red), and benthic $\delta^{13}C$ (blue), (c) Zr/Sr (black) and Si/Sr (brown) from X-ray fluorescence (XRF) core scanning.

Feinberg, 2008] to the remaining signal (using smoothing factor 12). The resulting smoothed and extrapolated background (detrital) signal was subtracted from the total FORC distribution to isolate the ridge signal (Figure 10b). The ridge signal (light green in Figure 9c) provides a measure of the varying SD concentration. The detrital (background) fraction from the ridge extraction procedure, expressed as [Detrital/(SD + Detrital)] (red in Figure 9c) mimics the M_r/M_s parameter (Figure 9c).

PCA analyses of FORCs demonstrate that the first two principal components describe most (83.5%) of the variability in the FORC data, hence we employed an unmixing model with three end-members (EMs) to characterize the system (Figure 11). One EM comprises the SD fraction (EM2, representative of bacterial magnetosomes), with resulting concentration (dark green in Figure 9c) that agrees with the results of the ridge extraction method (light green in Figure 9c). The other two EMs comprise the detrital fraction: EM1 represents the PSD component (~1–5 μm grains) and EM3 represents the MD component (~5–20 μm grains). The concentrations of these detrital fractions are plotted in Figure 9c (black triangles: MD, orange squares: PSD).

Quantitative FORC analysis demonstrates that the change in bulk magnetic grain-size parameters (κ_{ARM}/κ and M_r/M_s) observed over Termination I (Figure 9) are the result of a change in the relative proportions of two distinct magnetic components, bacterial SD magnetosomes versus detrital (PSD and MD) grains, rather than a decrease in the average grain size of a single magnetite population. The analysis reveals that the change in bulk magnetic grain-size parameters is explained entirely by the decreasing concentration of detrital magnetite. The magnetic contribution from SD biogenic magnetosomes (the ridge signal) remains more or less constant in the interval covered by the FORCs (Figure 9c), based on both the ridge extraction and PCA methods of analysis.

7. TEM Observations

For transmission electron microscopy (TEM), a magnetic extract from the Holocene of Core MD04-2822 (11–15 cm below seafloor) was prepared by sonicating ~20 cm^3 of sediment in a sodium metaphosphate dispersant. The solution was transferred to a reservoir feeding a circulating system driven by a peristaltic pump that allowed the fluid to pass slowly past the outside of a test-tube containing a rare-earth magnet. The material that adhered to the outside of the test-tube was then removed to a methanol solution using a

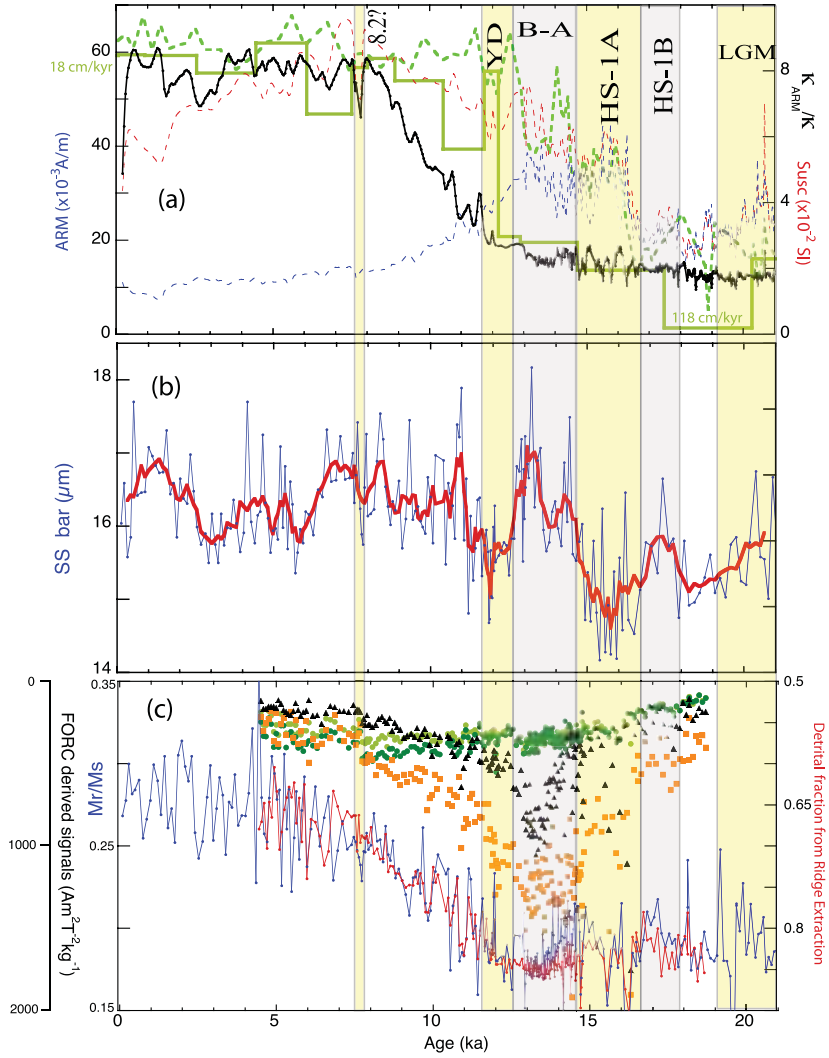

Figure 9. Core MD04-2822 Termination I: (a) The κ_{ARM}/κ (black), volume susceptibility (red dashed with scale, increasing down-plot, not shown), and ARM intensity (blue dashed) compared with benthic $\delta^{18}O$ (light green-dashed line with scale, increasing down-plot, not shown) and sedimentation rate changes (green) from ~118 cm/kyr at 21 ka to ~18 cm/kyr in the late Holocene. (b) Mean grain-size of sortable silt (blue) and after 5-point smoothing (red). (c) The saturation remanence over saturation magnetization ratio (Mr/Ms, blue) compared with results from FORC analysis using the ridge extraction method: single domain (SD) ridge signal (light green) and background (detrital) fraction expressed as Detrital/(SD + Detrital) (red line). Concentration of end-members (EMs) using FORC principal component analysis (FORC-PCA): SD (EM2: dark green circles), PSD (EM1: orange squares), MD (EM3: black triangles). The 8.2 Event, Younger Dryas (YD), Bølling-Allerød (B-A), Heinrich stadials HS-1A and HS-1B, and last glacial maximum (LGM) are marked.

methanol squeeze-bottle. Grains of magnetic separate were encouraged to adhere to a 3 mm copper TEM grid using another magnet suspended a few centimeters above the TEM grid floating at the surface of the methanol solution. Observations were made using a JEOL JEM-2010F high-resolution (HR) TEM in conjunction with energy dispersive X-ray spectroscopy (EDS) at an accelerating voltage of 200 kV. The microscope is equipped with a Gatan MultiScan Camera Model 794 for imaging and an Oxford Instruments detector with INCA 4.05 software for microanalysis. Spot analyses were conducted in STEM mode with a nominally ~1 nm probe size and a camera length of 12 cm.

Observation of the Holocene magnetic extract (Figure 12) indicated grains with shape and size typical for biogenic (bacterial) magnetite [e.g., *Vali et al.*, 1987; *Lean and McCave*, 1998; *Kopp and Kirschvink*, 2008; *Roberts et al.*, 2011, 2012; *Yamazaki*, 2012; *Channell et al.*, 2013]. Several EDS spectra derived from spots in the

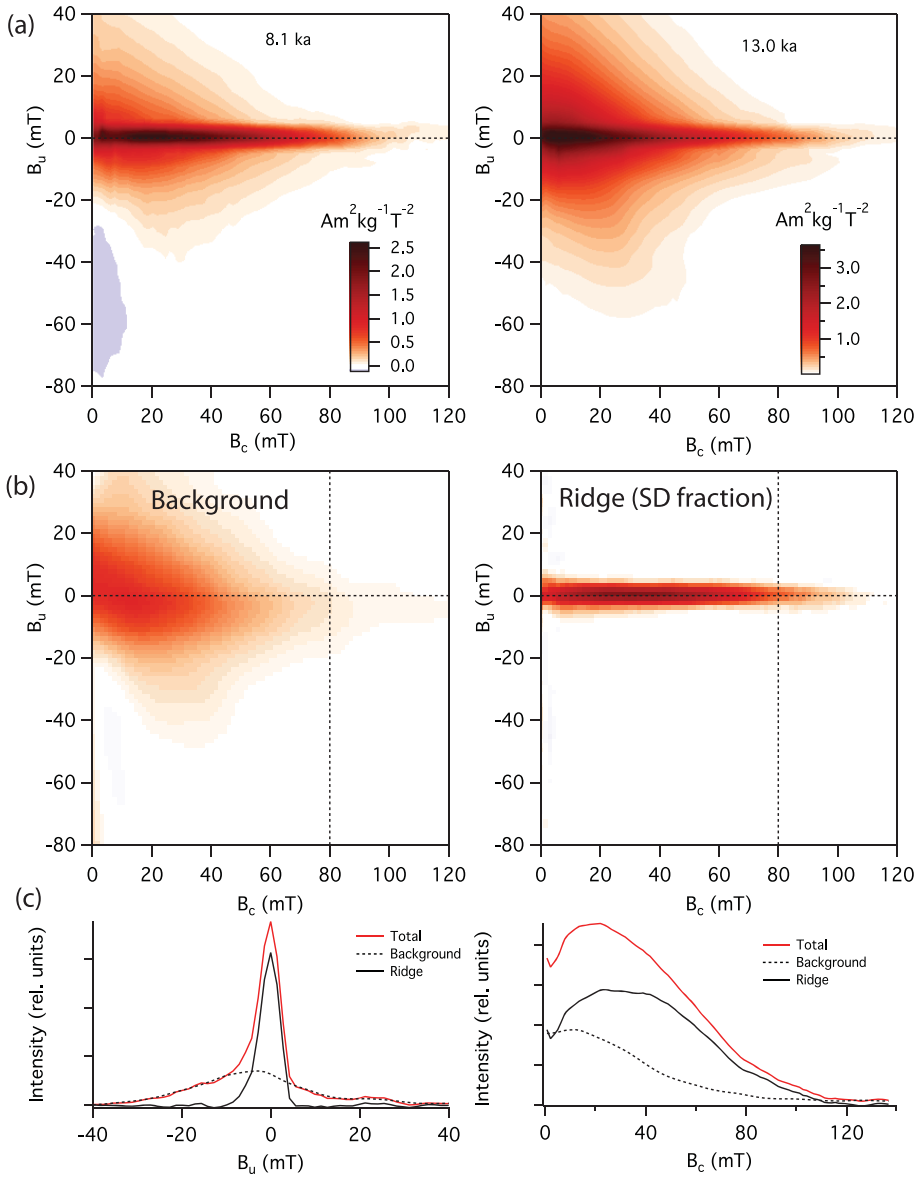

Figure 10. (a) FORC diagrams from 150 cm below seafloor (8.1 ka) and 298 cm below seafloor (13.0 ka) as end-members of the decrease in the detrital magnetite fraction in the 13–8 ka interval. (b) Left: Example of smoothed background signal obtained by applying locally weighted regression smoothing (SF = 12) to data outside the central ridge ($|B_u| < 5$ mT). Right: Example of extracted central ridge. Both examples from FORC at 13.0 ka. (c) Profiles along B_u axis at $B_c = 80$ mT (indicated by dashed vertical line in Figure 10b) for total (red), smoothed background (dashed) and extracted ridge (black) distributions. Profiles along B_c axis at $B_u = 0$ mT (indicated by dashed vertical line in Figure 10b) for total (red), smoothed background (dashed) and extracted ridge (black) distributions.

center of typically biogenic individual grains indicate that they contain Fe and O (including Cu from the TEM grid), but no Ti (Figure 12), a magnetite composition typical for bacterial magnetosomes but not for detrital titanomagnetite.

8. Discussion

Core MD04-2822 from the Rockall Trough has high sedimentation rate during MIS 2 and Termination I, combined with high-quality age control. The directional magnetic record features an apparent magnetic excursion at ~16 mbsf that occupies about 35 cm of core (Figures 3 and 5). U-channel samples, after AF

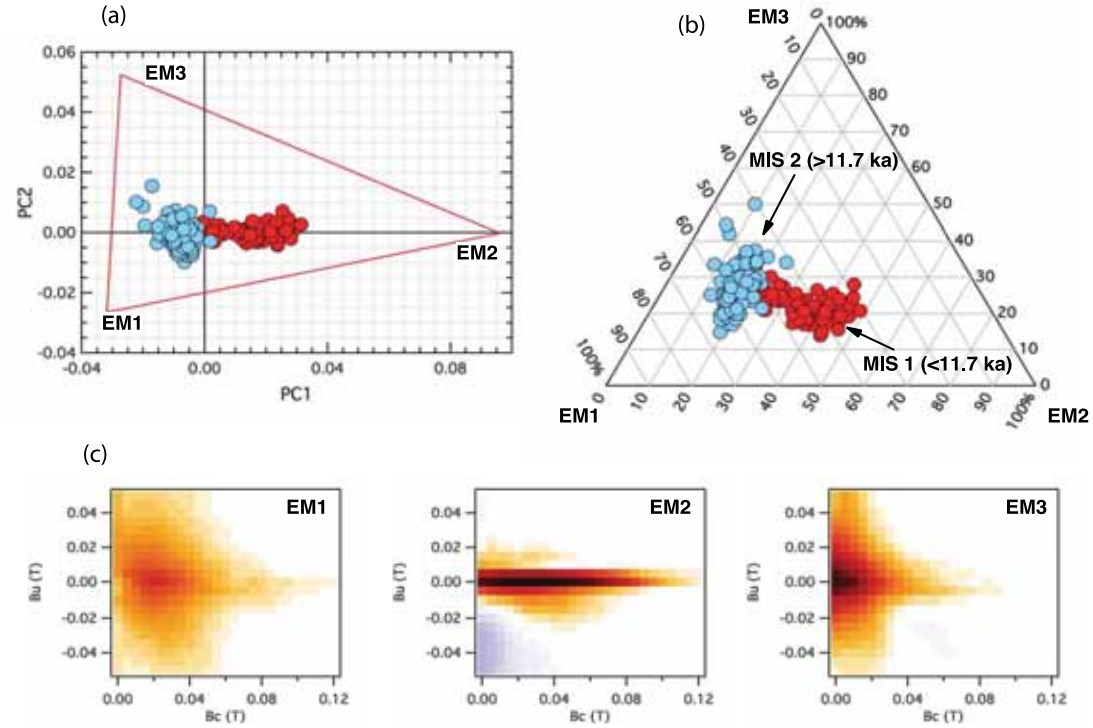

Figure 11. Principal component analysis (PCA) and unmixing model for samples from the 4.5–18.5 ka interval in Core MD04-2822. (a) PCA score plot and unmixing model boundary (red triangle). Vertices represent end-members (EMs). (b) Ternary diagram showing relative abundances of the three EMs. (c) Computed FORC diagrams for EM1 (PSD magnetite), EM2 (SD magnetite), and EM3 (MD magnetite). Red and blue symbols in Figures 11a and 11b represent Holocene (MIS 1, <11.7 ka), and Late Pleistocene (MIS 2, >11.7 ka) samples, respectively.

demagnetization, and cubic 7 cm^3 discrete samples, after AF and thermal demagnetization, indicate the presence of component magnetization directions that have steep negative inclination (Figure 4), and are close to reverse polarity with virtual geomagnetic poles (VGPs) at high southerly latitudes (Figure 5). The age model implies an age for the midpoint for the "Rockall" excursion of 26.5 ka and a duration for the excursion of ~350 years (Figure 5).

The Laschamp excursion at ~41 ka is the best documented of all magnetic excursions, and is well known from widely distributed sedimentary deep-sea cores [e.g. *Laj et al*., 2000, 2006; *Channell*, 2006; *Channell et al*., 2000; *Mazaud et al*., 2002; *Lund et al*., 2005; *Channell et al*., 2013] and volcanic rocks exposed on land in France [e.g., *Laj et al*., 2014], and has duration of <1 kyr. Magnetic excursions younger than the Laschamp excursion are controversial. The excursion recorded at Wilson Creek (Mono Lake) was originally referred to as the "Mono Lake excursion" and has usually been assigned an age of ~32 ka based on radiocarbon ages from the Great Basin [*Liddicoat and Coe*, 1979; *Benson et al*., 2003; *Cassata et al*., 2010]. In recent years, a body of evidence has accumulated that the excursion recorded at Wilson Creek is, in fact, coeval with the Laschamp excursion [*Kent et al*., 2002; *Zimmerman et al*., 2006; *Cox et al*., 2012; *Vazquez and Lidzbarski*, 2012] implying that the radiocarbon ages from the Mono Lake region are biased by recent contamination. On the other hand, excursions at ~32 ka have been recorded in the North Atlantic [*Channell*, 2006], in volcanic rocks from New Zealand [*Cassata et al*., 2008]) and Tenerife [*Kissel et al*., 2011], and in the Great Basin of California outside Wilson Creek [*Benson et al*., 2013; *Negrini et al*., 2014]. In deep boreholes (SOH1 and SOH4) that recovered several hundred meters of basalt from Hawaii, *Teanby et al*. [2002] found several intervals where NRM components have negative inclinations, at ~20, ~35, and ~40 ka. The K-Ar and Ar/Ar age control has low resolution due to low potassium content of the basalts, and ages are therefore poorly constrained. *Teanby et al*. [2002] associated the youngest of the three negative-inclination intervals with an anomalously low site-mean inclination (8.5° versus ~35°) from Hilina Pali, Hawaii [*Coe et al*., 1978] that had a radiocarbon age of ~18 ka [*Rubin and Berthold*, 1961]. The two older intervals of negative inclination from the SOH1 and SOH4 boreholes (Hawaii) were associated with the Mono Lake excursion and the Laschamp

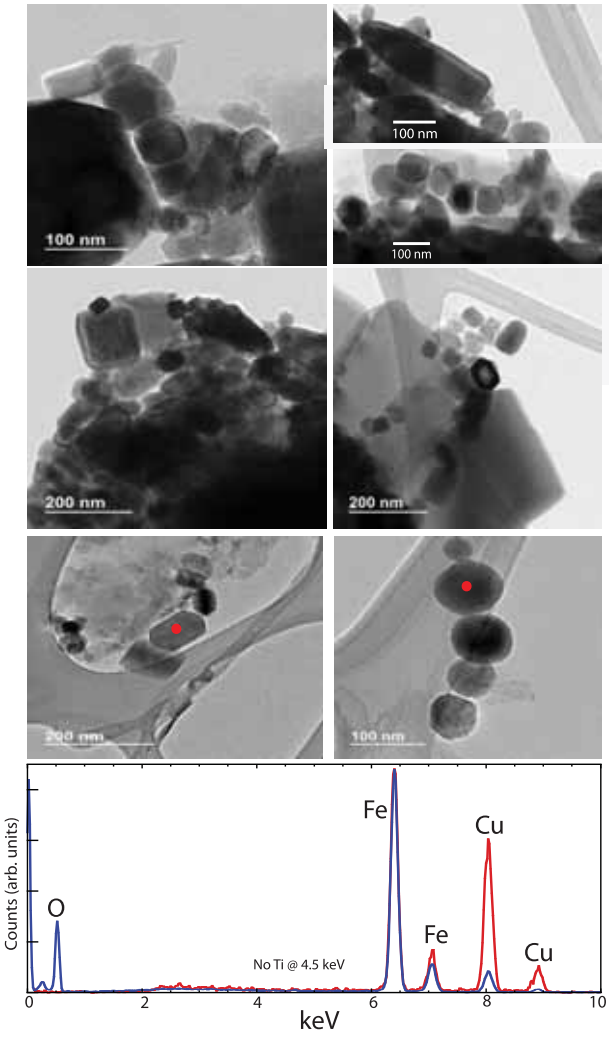

Figure 12. Photomicrographs from transmission electron microscopy (TEM) of a magnetic extract from the Holocene of Core MD04-2822 (11–15 cm below seafloor). Energy-dispersive X-ray spectroscopy (EDS) spectra for (red) spots at the center of two bacterial magnetosomes indicate Fe and O (including Cu from the TEM grid), but no Ti.

excursion [*Teanby et al.*, 2002]. Finally, *Zhu et al.* [2000] recorded an apparent excursion in a thick flow from the Tianchi Volcano (China) that has been recently dated using $^{40}Ar/^{39}Ar$ methods to 17 ka, associated with Hilina Pali, and labeled the Hilina Pali/Tianchi excursion [*Singer et al.*, 2014]. The results of this paper add another potential excursion (the "Rockall" excursion at ~26 ka) to the confusing picture of possible post-Laschamp magnetic excursions. The apparent duration of the "Rockall" excursion (~350 years) is such that it is unlikely that it would be recorded at normal pelagic sedimentation rates (<20 cm/kyr) due to the smoothing effects of bioturbation and a finite magnetization lock-in zone below the uppermost bioturbated layer. The high sedimentation rates in the 13–30 ka interval in Core MD04-2822 (Figure 2), and the uniform silty clay lithology, have apparently facilitated the recording of this putative magnetic excursion.

Alternating field and thermal demagnetization of u-channels and discrete samples (Figure 4), other magnetic parameters (Figure 7), and TEM observations (Figure 12) indicate that the magnetizations in Cores MD04-2822 are carried by a mixture of detrital (PSD and MD) magnetite and bacterial SD magnetite (magnetosomes). FORC diagrams show a combination of a prominent ridge along the horizontal B_c axis, superimposed on a vertically and horizontally spread background (Figure 10a). The horizontal ridge (also known as the central ridge) is diagnostic of noninteracting uniaxial SD grains [*Newell*, 2015; *Egli et al.*, 2010; *Harrison and Lascu*, 2014], and samples that contain magnetosomes [e.g. *Egli et al.*, 2010; *Roberts et al.*, 2011, 2012; *Yamazaki*, 2012; *Channell et al.*, 2013]. Partly on the basis of TEM observations (Figure 12), we can associate the central ridge with the presence of magnetosome relics of magnetotactic bacteria, and the background signal with detrital PSD + MD (titano)magnetite. Two methods of analysis of FORC diagrams (ridge extraction and FORC-PCA) over Termination I in Core MD04-2822 indicate that decreasing concentration of the detrital fraction accounts for the bulk magnetic grain-size decrease (as measured by κ_{ARM}/κ and M_r/M_s), and that the SD (magnetosome) fraction is relatively constant over the measured interval (Figure 9c). The change in magnetic grain size denoted by bulk parameters κ_{ARM}/κ and M_r/M_s immediately postdates an abrupt sixfold drop in sedimentation rate from ~118 to ~18 cm/kyr (Figure 9).

Although the κ_{ARM}/κ and M_r/M_s ratios track the detrital signal in the 5–12 ka interval, these ratios fail to reflect the large variations in absolute EM signals that are observed prior to 15 ka. FORC-PCA provides a more fundamental tracer of magnetic variations in these sediments than traditional grain-size proxies.

Ratios such as κ_{ARM}/κ and M_r/M_s can be linked to (and, in principle, entirely derived from) the absolute EM signals identified by FORC-PCA. This principle is illustrated by the excellent agreement between M_r/M_s and the FORC-derived detrital fraction from ridge extraction [Detrital/(SD + Detrital)] (red in Figure 9c). Examination of the absolute EM signals, however, reveals a more comprehensive picture of the magnetic variations that occur throughout the core, which correlates well with inferred geological processes. The FORC-PCA method indicates a trend within MIS 2 of varying proportions of PSD and MD detrital grains, and within MIS 1 (<11.7 ka) a decreasing trend of the PSD + MD (detrital) fraction (Figure 11). Elevated MD magnetite concentrations during the Bølling-Allerød warm period are consistent with enhanced bottom-current velocity from the mean grain size of sortable silt (Figure 9b and c). High PSD + MD magnetite concentration within HS-1A at 16.1 ka (Figure 9c) coincides with increased concentrations of ice-rafted debris (IRD) associated with H1 [e.g., *Scourse et al.*, 2009]. A small peak is observed exclusively in the PSD signal at 12.1 ka, which may be associated with the Vedde ash. Prior the Bølling-Allerød warm period, during HS-1A and HS-1B, a slight decrease with age in SD and MD magnetite concentration is accompanied by a more marked decrease in the PSD magnetite concentration.

9. Conclusions

An apparent magnetic excursion at ~26.5 ka in Core MD04-2822, with duration of ~350 years, was found in u-channel samples, and in discrete samples after both AF and thermal demagnetization. This observation adds to the confusion surrounding magnetic excursions in the 15–30 ka interval, augmenting observations from Hawaii and China for the presence of a magnetic excursion in this interval. The excursion is associated with a minimum in the relative paleointensity (RPI) record (Figure 6) that can be correlated to a minimum in geomagnetic field intensity derived from cosmogenic isotope fluxes in Greenland ice cores [*Muscheler et al.*, 2005].

We demonstrate that FORC-PCA can be used to identify the absolute variations in magnetic contributions from physically identifiable EMs that can be linked to geological processes (e.g., bacterial production/magnetosome dissolution, bottom-current strength, detrital source, and IRD input). Magnetic grain-size sensitive parameters and ratios that are often measured (e.g., κ_{ARM}/κ and M_r/M_s) can be entirely derived from the fundamental EM signals, and, it could be argued, become superfluous after FORC-PCA analysis.

PCA-FORC analysis indicates that detrital (PSD + MD) magnetite concentrations increase into the Bølling-Allerød warm period and are progressively reduced from the onset of the Younger Dryas (~13 ka) to ~8 ka (Figure 9), leaving sediment that is increasingly dominated by the relatively constant SD biogenic (magnetosome) signal. We interpret the changes in magnetic parameters as being primarily linked to changes in sources of detritus carried to the site by bottom-currents.

From models of glacial rebound in the region, combined with paleodepth data from cores located south of St. Kilda on the Scottish continental shelf west of the Outer Hebrides, water depths began to increase at ~13 ka continuing until ~7 ka, with sea-level rise in this interval of ~70 m [*Lambeck*, 1995]. Contemporaneous with this sea-level rise, deep-water masses in the Rockall Trough likely switched from being dominated by SSW to being dominated by NEADW and LSW [*Curry and Oppo*, 2005]. The decrease in grain size of magnetite from 12 ka to 8 ka, and a similar decease at Termination II, lag benthic $\delta^{18}O$ and are more synchronous with benthic $\delta^{13}C$ and XRF ratios (Zr/Sr and Si/Sr) indicative of detrital input (Figure 8). The timing of magnetite grain-size fining (12–8 ka) is interpreted as due to the progressive shutdown of detrital sources linked to contemporaneous sea level rise and to contemporaneous bottom-water reorganization at ~2000 m water depth in the Rockall Trough, as northerly-sourced waters supplanted SSW.

Acknowledgments
Research supported by U.S. NSF grants 0850413 and 1014506, and the European R12esearch Council under the European Union's Seventh Framework Programme (FP/2007-2013)/ERC grant agreement 320750. The UK NERC and BGS funded the recovery of Core MD04-2822. We thank Kainian Huang for work in the paleomagnetic laboratory at the University of Florida, the Captain and crew of the *Marion Dufresne* for their support during recovery of Core MD04-2822, and Bryan Lougheed and an anonymous reviewer for thorough reviews of the manuscript. Data archived at the Pangaea Database (www.pangaea.de).

References

Armishaw, J. E., R. W. Holmes, and D. A. Stow (2000), The Barra Fan: A bottom-current reworked, glacially fed submarine fan system, *Mar. Pet. Geol.*, *17*, 219–238.

Austin, W. E. N., and F. D. Hibbert (2012), Tracing time in the ocean: A brief review of chronological constraints (60-8 kyr) on North Atlantic marine event-based stratigraphies, *Quat. Sci. Rev.*, *36*, 28–37.

Austin, W. E. N., E. Bard, J. B. Hunt, D. Kroon, and J. D. Peacock (1995), The ^{14}C age of the Icelandic Vedde Ash: Implications for Younger Dryas marine reservoir age corrections, *Radiocarbon*, *37*(1), 53–62.

Banerjee, S. K., J. King, and J. Marvin (1981), A rapid method for magnetic granulometry with applications to environmental studies, *Geophys. Res. Lett.*, *8*(4), 333–336.

Bazin, L. et al. (2013), An optimized multi-proxy, multi-site Antarctic ice and gas orbital chronology (AICC2012): 120-800 ka, *Clim. Past*, *9*(4), 1715–1731, doi:10.5194/cp-9-1715-2013.
Benson, L, J. Liddicoat, J. Smoot, A. Sarna-Wojcicki, R. Negrini, and S. Lund (2003), Age of the Mono Lake excursion and associated tephra, *Quat. Sci. Rev.*, *22*, 135–140.
Benson, L., J. Smoot, S. Lund, S. Mensing, F. Foit Jr., and R. Rye (2013), Insights from a synthesis of old and new climate-proxy data from the Pyramid and Winnemucca lake basins for the period 48–11.5 cal ka, *Quat. Int.*, *310*, 62–82, doi:10.1016/j.quaint.2012.02.040.
Bianchi, G. G., I. R. Hall, I. N. McCave, and L. Joseph (1999), Measurement of the sortable silt current speed proxy using the Sedigraph 5100 and Coulter Multisizer IIe: Precision and accuracy, *Sedimentology*, *46*, 1001–1014.
Bronk Ramsey, C. (2008) Deposition models for chronological records, *Quat. Sci. Rev.*, *27*, 42–60.
Bronk Ramsey, C., and S. Lee (2013), Recent and planned development of the program OxCal, *Radiocarbon*, *55*(2–3), 720–730.
Brown, L., G. T. Cook, A. B. MacKenzie, and J. Thompson (2001), Radiocarbon age profiles and size dependency of mixing in northeast Atlantic sediments, *Radiocarbon*, *43*(2B), 929–937.
Carter-Stiglitz, B., B. Moskowitz, and M. Jackson (2001), Unmixing magnetic assemblages and the magnetic behavior of bimodal mixtures, *J. Geophys. Res.*, *106*(26), 397–411.
Cassata, W., B. Singer, and J. Cassidy (2008), Laschamp and Mono Lake excursions recorded in New Zealand, *Earth Planet. Sci. Lett.*, *268*, 76–88.
Cassata, W., B. Singer, J. Liddicoat, and R. Coe (2010), Reconciling discrepant chronologies for the geomagnetic excursion in the Mono Basin, California: Insights from new $^{40}Ar/^{39}Ar$ dating experiments and a revised paleointensity correlation, *Quat. Geochron.*, *5*, 533–543.
Channell, J. E. T. (2006), Late Brunhes polarity excursions (Mono Lake, Laschamp, Iceland Basin and Pringle Falls) recorded at ODP Site 919 (Irminger Basin), *Earth Planet. Sci. Lett.*, *244*, 378–393.
Channell, J. E. T., and Y. Guyodo (2004), The Matuyama chronozone at ODP Site 982 (Rockall Bank): Evidence for decimeter-scale magnetization lock-in depths, in *Timescales of the Paleomagnetic Field, AGU Geophys. Monogr.*, vol. 145, edited by J. E. T. Channell et al., 205–219, AGU, Washington, D. C.
Channell, J. E. T., J. S. Stoner, D. A. Hodell, and C. D. Charles (2000), Geomagnetic paleointensity for the last 100 kyr from the subantarctic South Atlantic: A tool for inter-hemispheric correlation, *Earth Planet. Sci. Lett.*, *175*, 145–160.
Channell, J. E. T., C. Xuan, and D. A. Hodell (2009), Stacking paleointensity and oxygen isotope data for the last 1.5 Myrs (PISO-1500), *Earth Planet. Sci. Lett.*, *283*, 14–23.
Channell, J. E. T., D. A. Hodell, and J. H. Curtis (2012), ODP Site 1063 (Bermuda Rise) revisited: Oxygen isotopes, excursions and paleointensity in the Brunhes Chron, *Geochem. Geophys. Geosyst.*, *13*, Q02001, doi:10.1029/2011GC003897.
Channell, J. E. T., D. A. Hodell, V. Margari, L. C. Skinner, P. C. Tzedakis, and M. S. Kesler (2013), Biogenic magnetite, detrital hematite, and relative paleointensity in sediments from the Southwest Iberian Margin, *Earth Planet. Sci. Lett.*, *376*, 99–109.
Channell, J. E. T., J. D. Wright, A. Mazaud, and J. S. Stoner (2014), Age through tandem correlation of Quaternary relative paleointensity (RPI) and oxygen isotope data at IODP Site U1306 (Eirik Drift, SW Greenland), *Quat. Sci. Rev.*, *88*, 135–146.
Coe, R. S., S. Grommé, and E. A. Mankinen (1978), Geomagnetic paleointensities from radiocarbon-dated lava flows on Hawaii and the question of the Pacific non-dipole low, *J. Geophys. Res.*, *83*(B4), 1740–1756.
Cox, S. E., K. A. Farley, and S. R. Hemming (2012), Insights into the age of the Mono Lake Excursion and magmatic crystal residence time from (U-Th)/He and Th-230 dating of volcanic allanite, *Earth Planet. Sci. Lett.*, *319*, 178–184.
Croudace, I. W., A. Rindby, and R. G. Rothwell (2006), ITRAX: Description and evaluation of a new multifunction X-ray core scanner, in *New Techniques in Sediment Core Analysis, Geol. Soc. London, Spec. Pub.*, vol. 267, edited by R. G. Rothwell, pp. 51–63, Geol. Soc. of London, U. K.
Curry W. B., and D. W. Oppo (2005), Glacial water mass geometry and the distribution of $\delta^{13}C$ of ΣCO_2 in the western Atlantic Ocean, *Paleoceanography*, *20*, PA1017, doi:10.1029/2004PA001021.
Day, R., M. Fuller, and V. A. Schmidt (1977), Hysteresis properties of titanomagnetites: Grain-size and compositional dependence, *Phys. Earth Planet. Int.*, *13*, 260–267.
Dunlop, D. J. (2002), Theory and application of the Day plot (M_{rs}/M_s versus H_{cr}/H_c) 1. Theoretical curves and tests using titanomagnetite data, *J. Geophys. Res.*, *107*(B3), 2056, doi:10.1029/2001JB000486.
Dunlop, D. J. and B. Carter-Stiglitz (2006), Day plots of mixtures of superparamagnetic, single domain, pseudosingle domain, and multidomain magnetites, *J. Geophys. Res.*, *111*, B12S09, doi:10.1029/2006JB004499.
Egli, R. (2013), VARIFORC: An optimized protocol for calculating non-regular first-order reversal curve (FORC) diagrams, *Global Planet. Change*, *110*, 302–320, doi:10.1016/j.gloplacha.2013.08.003.
Egli, R., A. P. Chen, M. Winklhofer, K. P. Kodama and C-S. Horng (2010), Detection of noninteracting single domain particles using first-order reversal curve diagrams, *Geochem. Geophys. Geosyst.*, *11*, Q01Z11, doi:10.1029/2009GC002916.
Guyodo, Y., J. E. T. Channell, and R. Thomas (2002), Deconvolution of u-channel paleomagnetic data near geomagnetic reversals and short events, *Geophys. Res. Lett.*, *29*(17), 1845, doi:10.1029/2002GL014963.
Harkness, D. D. (1983), The extent of the natural 14C deficiency in the coastal environment of the United Kingdom, *J. Eur. Stud. Group Phys. Chem. Math. Tech. Appl. Archaeol. PACT*, *8*(IV.9), 351–364.
Harrison, R. J. and J. M. Feinberg (2008), FORCinel: An improved algorithm for calculating first-order reversal curve distributions using locally weighted regression smoothing, *Geochem. Geophys. Geosyst.*, *9*, Q05016, doi:10.1029/2008GC001987.
Harrison, R. J., and I. Lascu (2014), FORCulator: A micromagnetic tool for simulating first-order reversal curve diagrams, *Geochem. Geophys. Geosyst.*, *15*, 4671–4691, doi:10.1002/2014GC005582.
Häykansson, S. (1984), A reservoir age for the coastal waters of Iceland, *Geologiska Föreningens i Stockholm Förhandlinger*, *105*, 64–67.
Heslop, D. (2009), On the statistical analysis of the rock magnetic S-ratio, *Geophys. J. Int.*, *178*, 159–161.
Hibbert, F. D., W. E. N. Austin, M. J. Leng, and R. W. Gatliff (2010), British ice sheet dynamics inferred from North Atlantic ice-rafted debris records spanning the last 17 500 years, *J. Quat. Sci.*, *25*, 461–482.
Hibbert, F. D., S. Wastegard, R. Gwynn, and W. E. N. Austin (2014), Identification of a MIS 6 age (c. 180 ka) Icelandic tephra within NE Atlantic sediments: A new potential chronostratigraphic marker, in, *Marine Tephrochronology*, edited by W. E. N. Austin, *Geol. Soc. Spec. Publ.*, 398, 65–80. [Available at http://dx.doi.org/10.1144/SP398.10.]
Kent D. V., S. R. Hemming, and B. D. Turrin (2002), Laschamp excursion at Mono Lake?, *Earth Planet. Sci. Lett.*, *197*, 151–164.
King, J. W., S. K. Banerjee, and J. Marvin (1983), A new rock-magnetic approach to selecting sediments for geomagnetic paleointensity studies: Application to paleointensity for the last 4000 years, *J. Geophys. Res.*, *88*(B7), 5911–5921.[10.1029/JB088iB07p05911]
Kirschvink, J. L. (1980), The least squares lines and plane analysis of paleomagnetic data, *Geophys. J. R. Astron. Soc.*, *62*, 699–718.
Kissel C., C. Laj, L. Labeyrie, T. Dokken, A. Voelker, and D. Blamart (1999), Rapid climatic variations during marine isotopic stage 3: Magnetic analysis of sediments from Nordic seas and north Atlantic, *Earth Planet. Sci. Lett.*, *171*, 489–502.

Kissel, C., C. Laj, T. Mulder, C. Wandres, and M. Cremer (2009), The magnetic fraction: A tracer of deep water circulation in the North Atlantic, *Earth Planet. Sci. Lett.*, *288*, 444–454.
Kissel C., H. Guillou, C. Laj, J. C. Carracedo, S. Nomade, F. Perez-Torrado, and C. Wandres (2011), The Mono Lake excursion recorded in phonolitic lavas from Tenerife (Canary Islands): Paleomagnetic analyses and coupled K/Ar and Ar/Ar dating, *Phys. Earth Planet. Int.*, *187*, 232–244, doi:10.1016/j.pepi.2011.04.014.
Kissel, C., A. Van Toer, C. Laj, E. Cortijo, and E. Michel (2013), Variations in strength of the North Atlantic bottom water during the Holocene, *Earth Planet. Sci. Lett.*, *369–370*, 248–259.
Knutz, P. C., W. E. N. Austin, and E. J. W. Jones (2001), Millennial-scale depositional cycles related to British Ice Sheet variability and North Atlantic paleocirculation since 45 kyr B.P., Barra Fan, U.K. margin, *Paleoceanography*, *16*(1), 53–64.
Knutz, P. C., E. J. W. Jones, W. E. N. Austin, and T. C. E. van Weering (2002), Glacimarine slope sedimentation, contourite drifts and bottom current pathways on the Barra Fan, UK North Atlantic margin, *Mar. Geol.*, *188*, 129–146.
Kopp, R. E., and J. L. Kirschvink (2008), The identification and biogeochemical interpretation of fossil magnetotactic bacteria, *Earth Sci. Rev.*, *86*, 42–61.
Laj, C., and J. E. T. Channell (2007),Geomagnetic excursions, in *Treatise on Geophysics*, vol. 5, Geomagnetism, chap. 10, edited by M. Kono, pp. 373–416, Elsevier, Amsterdam, Netherlands.
Laj, C., C. Kissel, A. Mazaud, J. E. T. Channell, and J. Beer (2000), North Atlantic paleointensity stack since 75 ka (NAPIS-75) and the duration of the Laschamp event, *Philos. Trans. R. Soc. London*, *358*, 1009–1025.
Laj, C., C. Kissel, and A. P. Roberts (2006), Geomagnetic field behavior during the Icelandic Basin and Laschamp geomagnetic excursions: A simple transitional field geometry?, *Geochem. Geophys. Geosyst.*, *7*, Q03004, doi:10.1029/2005GC001122.
Laj, C., H. Guillou, and C. Kissel (2014), Dynamics of the Earth's magnetic field in the 10-75 kyr period comprising the Laschamp and Mono Lake excursions: New results from the French Chaine des Puys in a global perspective, *Earth Planet. Sci. Lett.*, *387*, 184–197.
Lambeck, K. (1995), Glacial isostasy and water depths in the late Devensian and Holocene on the Scottish Shelf west of the Outer Hebrides, *J. Quat. Sci.*, *10*(1), 83–86.
Lascu, I., R. J. Harrison, Y. Li, J. R. Muraszko, J. E.T. Channell, A. M. Piotrowski, and D. A. Hodell (2015), Magnetic unmixing of first-order reversal curve diagrams using principal component analysis, *Geochem. Geophys. Geosyst.*, *16*, 2900–2915, doi:10.1002/2015GC005909.
Lean, C. M. B., and I. N. McCave (1998), Glacial to interglacial mineral magnetic and paleoceanographic changes at Chatham Rise, SW Pacific, *Earth Planet. Sci. Lett.*, *163*, 247–260.
Liddicoat, J. C., and R. S. Coe (1979), Mono Lake geomagnetic excursion, *J. Geophys. Res.*, *84*(B1), 261–271.
Lisiecki, L. E., and M. E. Raymo (2005), A Pliocene-Pleistocene stack of 57 globally distributed benthic d^{18}O records, *Paleoceanography*, *i*, PA1003, doi:10.1029/2004PA001071.
Lowrie, W. (1990), Identification of ferromagnetic minerals in a rock by coercivity and unblocking temperature properties, *Geophys. Res. Lett.*, *17*(2), 159–162.[10.1029/GL017i002p00159]
Lund, S. P., M. Schwartz, L. Keigwin, and T. Johnson (2005), Deep-sea sediment records of the Laschamp geomagnetic field excursion (<41,000 calendar years before present), *J. Geophys. Res.*, *110*, Q12006, doi:10.1029/2005GC001036.
Mazaud, A., M. A. Sicre, U. Ezat, J. J. Pichon, J. Duprat, C. Laj, C. Kissel, L. Beaufort, E. Michel, and J. L. Turon (2002), Geomagnetic-assisted stratigraphy and sea surface temperature changes in core MD94-103 (Southern Indian Ocean): Possible implications for North-South climatic relationships around H4, *Earth Planet. Sci. Lett.*, *201*, 159–170.
McCave, I. N., and I. R. Hall (2006), Size sorting in marine muds: Processes, pitfalls and prospects for palaeoflow-speed proxies, *Geochem. Geophys. Geosyst.*, *7*, Q10N05, doi:10.1029/2006GC001284.
McCave, I. N., B. Manighetti, and S. G. Robinson (1995), Sortable silt and fine sediment size/composition slicing: Parameters for palaeocurrent speed and palaeoceanography, *Paleoceanography*, *10*(3), 593–610.
Muscheler, R., J. Beer, P. W. Kubik, and H.-A. Synal (2005), Geomagnetic field intensity during the last 60,000 years based on ^{10}Be and ^{36}Cl from the summit ice cores and ^{14}C, *Quat. Sci. Rev.*, *24*, 1849–1860.
Muxworthy, A. R., and A. P. Roberts (2007), First-order reversal curve (FORC) diagrams, in *Encyclopedia of Geomagnetism and Paleomagnetism*, edited by D. Gubbins and E. Herrero-Bervera, pp. 266–272, Springer, Dordrecht, Netherlands.
Negrini, R. M., et al. (2014), Nongeocentric axial dipole field behavior during the Mono Lake excursion, *J. Geophys. Res. Solid Earth*, *119*, 2567–2581, doi:10.1002/2013JB010846.
New, A., and D. Smythe-Wright (2001), Aspects of the circulation in the Rockall Trough, *Cont. Shelf Res.*, *21*, 777–810.
Newell, A. J. (2015), A high-precision model of first-order reversal curve (FORC) functions for single-domain ferromagnets with uniaxial anisotropy, *Geochem., Geophys. Geosyst.*, *6*, Q05010, doi:10.1029/2004GC000877.
Olsson, I. U. (1980), Uppsala natural radiocarbon measurements II, *Am J. Sci. Radiocarbon Supp.*, *2*, 112–128.
Pike, C. R., A. P. Roberts, and K. L. Verosub (1999), Characterizing interactions in fine magnetic particle systems using first order reversal curves, *J. Appl. Phys.*, *85*, 6660–6667, doi:10.1063/1.370176.
Rasmussen S., et al. (2014), A stratigraphic framework for abrupt climatic changes during the Last Glacial period based on three synchronized Greenland ice-core records: Refining and extending the INTIMATE event stratigraphy, *Quat. Sci. Rev.*, *106*, 14–28.
Reimer, P. J., et al. (2013), IntCal13 and Marine13 radiocarbon age calibration curves 0–50,000 years cal BP, *Radiocarbon*, *55*(4), 1869–1887.
Roberts, A. P., and M. Winklhofer (2004), Why are geomagnetic excursions not always recorded in sediments? Constraints from post-depositional remanent magnetization lock-in modeling, *Earth Planet. Sci. Lett.*, *227*, 334–359.
Roberts, A. P., C. R. Pike, and K. L. Verosub (2000), First-order reversal curve diagrams: A new tool for characterizing the magnetic properties of natural samples, *J. Geophys. Res.*, *105*(B12), 28,461–28,475.
Roberts, A. P, F. Florindo, G. Villa, L. Chang, L. Jovane, S. M. Bohaty, J. C. Larrasoana, D. Heslop, and J. D. Fitz Gerald (2011), Magnetotactic bacterial abundance in pelagic marine environments is limited by organic carbon flux and availability of dissolved iron, *Earth Planet. Sci. Lett.*, *310*, 441–452.
Roberts, A. P., L. Chiang, D. Heslop, F. Florindo, and J. C. Larrasoana (2012), Searching for single domain magnetite in the "pseudo-single-domain" sedimentary haystack: Implications of biogenic magnetite preservation for sediment magnetism and relative paleointensity determinations, *J. Geophys. Res.*, *117*, B08104, doi:10.1029/2012JB009412.
Rubin, M., and S. M. Berthold (1961), U.S. Geological Survey radiocarbon dates, VI, *Radiocarbon*, *3*, 86–98.
Scourse, J. D., A. I. Haapaniemi, E. Colmenero-Hidalgo, V. L. Peck, I. R. Hall, W. E. N. Austin, P. C. Knutz, and R. Zahn (2009), Growth, dynamics and deglaciation of the last British-Irish ice sheet: The deep-sea ice-rafted detritus record, *Quat. Sci. Rev.*, *28*, 3066–3084.
Singer, B. S., B. R. Jicha, H. He, and R. Zhu (2014), Geomagnetic field excursion recorded 17 ka at Tianchi Volcano, China: New ^{40}Ar/^{39}Ar age and significance, *Geophys. Res. Lett.*, *41*, 2794–2802, doi:10.1002/2014GL059439.
Skinner, L. C., and I. N. McCave (2003), Analysis and modeling of gravity and piston coring based on soil mechanics, *Mar. Geol.*, *199*, 181–204.

Snowball, I., and M. Moros (2003), Saw-tooth pattern of North Atlantic current speed during Dansgaard-Oeschger cycles revealed by the magnetic grain size of Reykjanes Ridge sediments at 59°N, *Paleoceanography*, *18*(2), 1026, doi:10.1029/2001PA000732.

Stoker, M. S. (1995), The influence of glacigenic sedimentation on slope-apron development on the continental margin of Northwest Britain, in *The Tectonics, Sedimentation and Paleoceanography of the North Atlantic Region*, edited by R. A. Scrutten et al., *Geol. Soc. Spec. Publ.*, *90*, 159–177.

Stoner, J. S., J. E. T. Channell, A. Mazaud, S. E. Strano, and C. Xuan (2013), The influence of high latitude flux lobes on the Holocene paleomagnetic record of IODP Site U1305 and the northern North Atlantic, *Geochem. Geophys. Geosyst.*, *14*, 4623–4646, doi:10.1002/ggge.20272.

Széréméta, N., F. Bassinot, Y. Balut, L. Labeyrie and M. Pagel (2004), Oversampling of sedimentary series collected by giant piston corer: Evidence and corrections based on 3.5-kHz chirp profiles, *Paleoceanography*, *19*, PA1005, doi:10.1029/2002PA000795.

Teanby, N., C. Laj, D. Gubbins, and M. Pringle (2002), A detailed paleointensity and inclination record from drill core SOH1 on Hawaii, *Phys. Earth Planet. Int.*, *131*, 101–140.

Thomas, R., Y. Guyodo, and J. E. T. Channell (2003), U-channel track for susceptibility measurements, *Geochem. Geophys. Geosyst.*, *4*(6), 1050, doi:10.1029/2002GC000454.

Vali, H., O. Forster, G. Amarantidis, and N. Petersen (1987), Magnetotactic bacteria and their magnetofossils in sediments, *Earth Planet. Sci. Lett.*, *86*, 389–400.

Vazquez J. A., and M. I Lidzbarski (2012), High-resolution tephrochronology of the Wilson Creek Formation (Mono Lake, California) and Laschamp event using U-238-Th-230 SIMS dating of accessory mineral rims, *Earth Planet. Sci. Lett.*, *357*, 54–67, doi:10.1016/j.epsl.2012.09.013.

Waelbroeck, C., J. C. Duplessy, E. Michel, L. Labeyrie, D. Paillard, and J. Duprat (2001), The timing of the last deglaciation in North Atlantic climate records, *Nature*, *412*(6848), 724–727.

Weeks, R., C. Laj, L. Endignoux, M. Fuller, A. Roberts, R. Manganne, E. Blanchard, and W. Goree (1993), Improvements in long-core measurement techniques: Applications in palaeomagnetism and palaeoceanography, *Geophys. J. Int.*, *114*, 651–662.

Xuan, C., and J. E. T. Channell (2009), UPmag: MATLAB software for viewing and processing u-channel or other pass-through paleomagnetic data, *Geochem. Geophys. Geosyst.*, *10*, Q10Y07, doi:1029/2009GC002584.

Yamazaki, T. (2012), Paleoposition of the intertropical convergence zone in the eastern Pacific inferred from glacial-interglacial changes in terregenous and biogenic magnetic mineral fractions, *Geology*, *40*, 151–154.

Zhu, R., Y. Pan, and R. S. Coe (2000), Paleointensity studies of a lava succession from Jilin Province, northeastern China: Evidence for the Blake event, *J. Geophys. Res.*, *105*(B4), 8305–8317.

Zimmerman, S. H., S. R. Hemming, D. V. Kent, and S. Y. Searle (2006), Revised chronology for late Pleistocene Mono Lake sediments based on paleointensity correlation to the global reference curve, *Earth Planet. Sci. Lett.*, *252*, 94–106.